From first- to second-order phase transitions in hybrid improper ferroelectrics through entropy stabilisation

Fernando Pomiro,[1] Chris Ablitt,[1] Nicholas Bristowe,[2] Arash A. Mostofi,[3] Coongjae Won,[4] Sang-Wook Cheong,[4,5] and Mark S. Senn[1,*]

[1] *Department of Chemistry, University of Warwick, Gibbet Hill, Coventry, CV4 7AL, United Kingdom.*

[2] *School of Physical Sciences, University of Kent, Canterbury, CT2 7NH, United Kingdom.*

[3] *Departments of Materials and Physics, and the Thomas Young Centre for Theory and Simulation of Materials, Imperial College London, Exhibition Road, London SW7 2AZ, United Kingdom.*

[4] *Laboratory for Pohang Emergent Materials and Max Plank POSTECH Center for Complex Phase Materials, Pohang University of Science and Technology, Pohang, Korea.*

[5] *Rutgers Center for Emergent Materials and Department of Physics and Astronomy, Rutgers University, Piscataway, New Jersey, USA.*

(Dated: June 12, 2020)

PACS numbers: 75.25.Dk, 77.80.B-

* m.senn@warwick.ac.uk

In Section I details of the parametrization of the distortion modes, the refinements and Rietveld fits for $Ca_3Ti_2O_7$ and $Ca_{2.15}Sr_{0.85}Ti_2O_7$ against Synchrotron data are given, along with the evolution of some refined parameters as a function of temperature. Section II gives information on pseudopotentials and additional plots pertaining to the first-principles simulations.

I. MODES AND REFINEMENTS DETAILS

A. $Ca_3Ti_2O_7$

A sudden increase of the Rwp value is observed between 1100 to 1250 K when fitting the data with a single $A2_1am$ phase model (see Fig. S1), returning to low values of Rwp at temperatures higher than 1200 K (Rwp = 8.82). This means that a good fit of the data to the $A2_1am$ model can be achieved both below and above the phase coexistence range, but this scenario does not explain the origin of the phase coexistence.

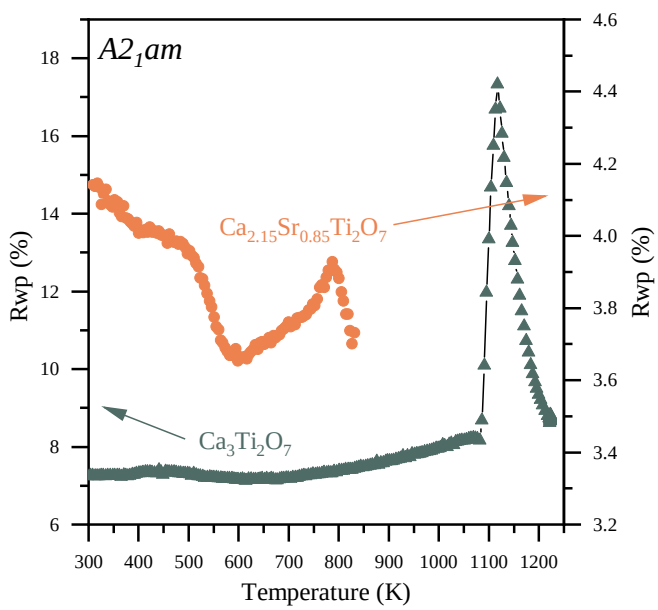

Figure S1. Comparison of the thermal evolution of the Rwp for $Ca_3Ti_2O_7$ and $Ca_{2.15}Sr_{0.85}Ti_2O_7$ when both set of data is refined with a single phase $A2_1am$ model. The small and gradual change in fitting statistic in $Ca_{2.15}Sr_{0.85}Ti_2O_7$ are consistent with a sequence of second order phase transitions as presented in the paper. While the abrupt change in fitting statistic observed in $Ca_3Ti_2O_7$ are consistent with a first order phase transition.

Additionally, we observe that at high temperature the $A2_1am$ model generates some spurious intensity not observed in the diffraction pattern (see Fig. S2). On the other hand, refinements performed at high temperature with the tetragonal aristotype $I4/mmm$ space group gave a considerably worse fit (Rwp = 9.65, see Fig. S2). After an extensive search of the isotropy subgroups of the parent structure compatible with the $[\frac{1}{2}, \frac{1}{2}, 0]$ propagation vector, we found that the $Acaa$ space group provides the best fit to the superstructure peaks with a Rwp = 8.78 (see Fig. S2). The agreement factors obtained with the $Acaa$ model are better than those obtained through the $A2_1am$ model whilst having considerably less parameters (see Table 1 in the main text). The $Acaa$ model is the same previously observed in the RP perovskite $Ca_3Mn_2O_7$ at room temperature [1, 2] and corresponds to an ordering of an X_1^-(a;0) mode, an out-of-phase rotation of the BO_6 octahedra along the c axis ($a^0a^0c^-/a^0a^0c^-$ in Glazer notation).

Fig. 1c in the main text display the thermal evolution of the c lattice parameters showing a clear discontinuity around the phase transition temperature and a decrease in the thermal expansion coefficient. Full thermal dependence of a, b and c lattice parameters are given via the .txt file that may be separately downloaded as part of the Supplemental Material.

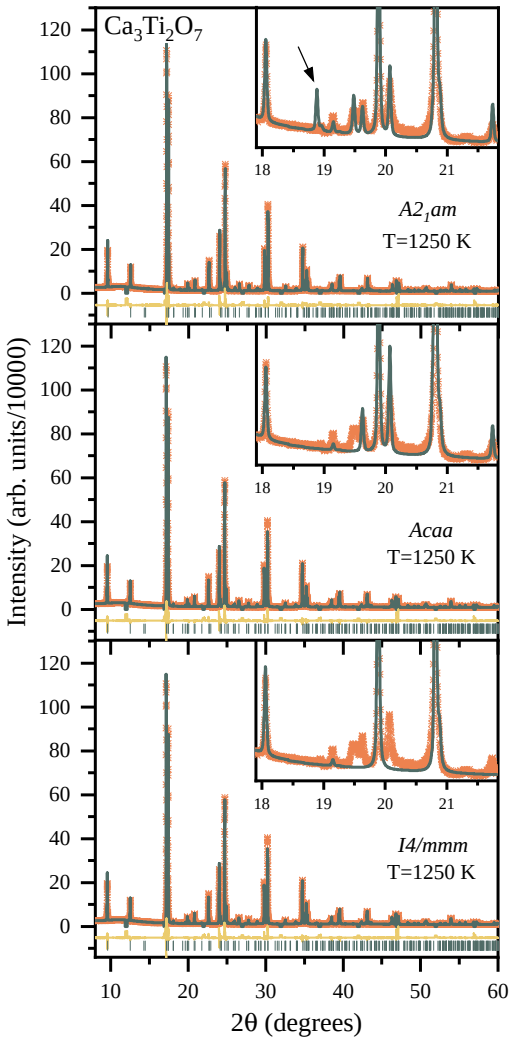

Figure S2. Rietveld fit to data collect on I11 for $Ca_3Ti_2O_7$ at 1250 K refined in the indicated models. Data points are plotted as orange crosses, Rietveld fit and differences as black and yellow lines respectively and black tick marks indicate symmetry allowed reflections. Inset shows enlarged region of the diffraction profile in the range 18-22 degrees. The arrow denoted the spurious reflection generating by the $A2_1am$ model. The broad peak that is not fitted with the *Acaa* model is present in the whole range of temperature and could be due to an impurity.

B. $Ca_{2.15}Sr_{0.85}Ti_2O_7$

Initially, we performed variable temperature refinements against the collected data with the $P2_1nm$ model, which is the highest symmetry subgroup to the $P4_2/mnm$, $Amam$, $Pnnm$ and $A2_1am$ models. With the proper symmetry constraints, this model capture all the likely symmetry braking (oxygen octahedra rotations and tilts) involved in the structural phase transitions from 300 to 900 K in $Ca_{2.15}Sr_{0.85}Ti_2O_7$ whilst in its unconstrained forms allows an unbiased refinement as presented below. First we observe at low temperatures that the X_2^+(a;0) mode amplitude (see Fig S4), which correspond to the in-phase rotation of the BO_6 octahedra along the c axes, decreases faster than the amplitude of the X_3^-(a;0) mode (out-of-phase tilting of the BO_6 octahedra in the ab plane) and the former is lost at around 550 K (see Fig S4). At this point, the evolution of the symmetry modes suggest a phase transition from the polar $A2_1am$ space group (X_2^+(a;0) $\oplus$ X_3^-(a;0), see Fig. 2a in the main text) to the paraelectric $Amam$ (X_3^-(a;0)). We notice also that whereas the amplitude of the a order parameter direction (OPD) of X_3^- decreases with temperature, the b OPD increases, reaching the same value $b = a$ at around 800 K (see Fig S4), exactly the same temperature where the unit cell become metrically tetragonal (see Fig. 2b in the main text). This equal values of the OPD a and b in X_3^- correspond to the tetragonal $P4_2/mnm$ space group. A second order transition scenario implies another

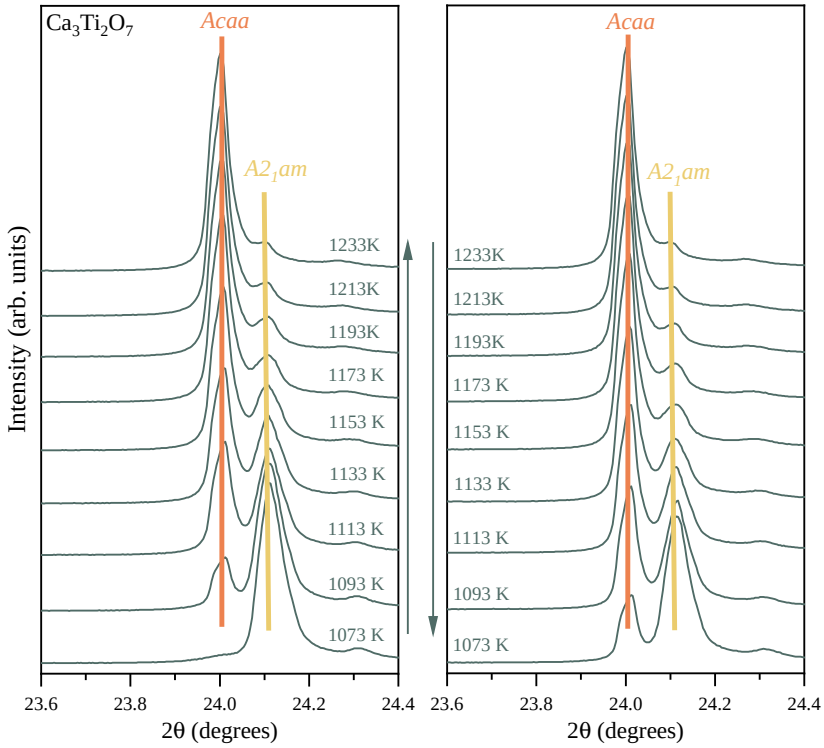

Figure S3. Temperature dependence of the two phases present in $Ca_3Ti_2O_7$ on warming and cooling. The phase coexistence reported in this sample can be easily observed following the vertical lines in the figure.

orthorhombic intermediate $Pnnm$ structure representing the X_3^- Irrep with *OPDs* (a;b), which is a sub-group of both $Amam$ and $P4_2/mnm$. In this case, a possible pathway of the transition could be $A2_1am \rightarrow Amam \rightarrow Pnnm \rightarrow P4_2/mnm \rightarrow I4/mmm$, as we show in Fig. 2a in the main text. The features observed in the thermal dependence of the mode amplitude are in good agreement with the changes observed in the thermal expansion coefficient of the c lattice parameter (see Fig. 2c in the main text) and consistent with the high symmetry *OPD* for the sequence of phase transitions that we present here.

Using the results from these unbiased refinement we then construct the correct symmetry constraints that describe the space groups of the distinct crystallographic phases that we have identified. These models are then refined against the high resolution MAC data as reported in the paper. FindSymm [3] is used to construct the final models from the refinement output that are expressed in the correct space group, and are available as .cif files as part of this Supplemental Material. As can be observed in the .str file, the $P2_1nm$ model has 12 degrees of freedom that correspond with the Irrep X3- and this order parameter is active in both of the doubly degenerate reciprocal space direction (X3-(a;b)). In the case of the $A2_1am$ and $Amam$ models, for example, the order parameter X3- is only active in one direction (X3-(a;0)), which mean that for these two model there are only 6 degrees of freedom that correspond with X3-.$P4_2/mnm$ (tetragonal) also has 6 degrees of freedom that correspond with X3-, but in this case is because both branches have the same value (X3-(a;a)). $Pnnm$ has 12 degrees of freedom corresponding with X3- and both direction are different (X3-(a;b)). In order to reduce the number of parameters in our refinements to make the comparison among the refinements with different models fairer we defined a new parameter call "branch" that relate the amplitude of the modes in the "a" (X3-(a;0)) and "b" (X3-(0;b)) order parameter directions. Physically this approximation can be viewed as being related to a harmonic approximation in which the character of the eigenvectors (phonon) of the undistorted parent structure are constant. So, in each case we refined only 6 parameters that correspond with X3- and the "branch" parameter. The "branch" parameter was fixed to 1 for the $P4_2/mnm$ model (X3-(a,a)) and fixed to 0 for $A2_1am$ and $Amam$ models (X3-(a,0)). Details of the structural models at each temperature are given via .cif files which may be separately downloaded as part of the Supplemental Material.

At 773 K we still observe some weak superstructure peaks at $(h{+}\frac{1}{2},\ k{+}\frac{1}{2},\ l)$, like $(\frac{3}{2}\frac{\bar{1}}{2}3)_T$ (T = aristotype tetragonal setting) and $(\frac{1}{2}\frac{1}{2}7)_T$ reflections in the $I4/mmm$ aristotype tetragonal setting that correspond with the $(213)_O$ (O = orthorhombic setting) and $(017)_O$ reflections in the orthorhombic setting, respectively (see Fig. S5). At this

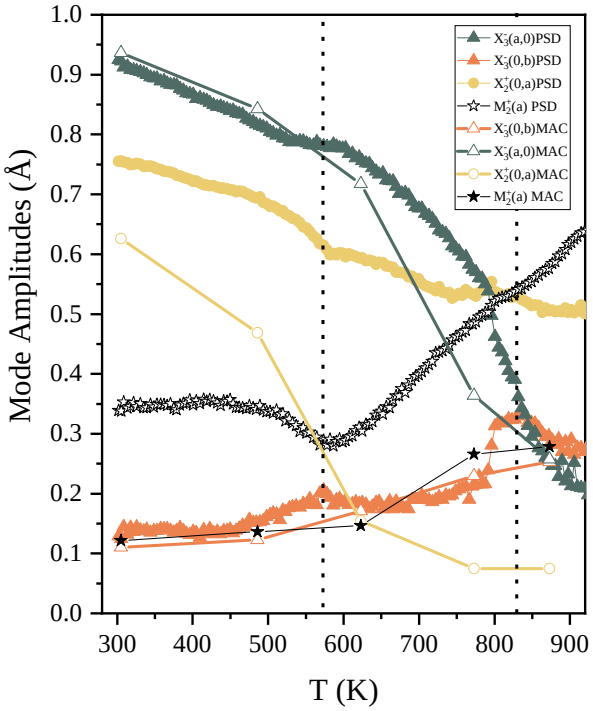

Figure S4. Thermal evolution of the distortion modes of symmetry X_3^- (a,0), X_3^-(0,b), X_2^+(0,a) and M_2^+ obtained refining the PSD and the MAC data with the unbiased $P2_1am$ model. We observe that the X_2^+(a;0) mode amplitude, which correspond to the in-phase rotation of the BO_6 octahedra along the c axes, decreases faster than the amplitude of the X_3^-(a;0) mode (out-of-phase tilting of the BO_6 octahedra in the ab plane) and the former is lost at around 550 K. At this point, the evolution of the symmetry modes suggest a phase transition from the polar $A2_1am$ space group (X_2^+(a;0) $\oplus$ X_3^-(a;0)) to the paraelectric $Amam$ (X_3^-(a;0)). We notice also that whereas the amplitude of the a order parameter direction (OPD) of X_3^- decreases with temperature, the b OPD increases, reaching the same value $b = a$ at around 800 K, exactly the same temperature where the unit cell become metrically tetragonal. This equal values of the OPD a and b in X_3^- correspond to the tetragonal $P4_2/mnm$ space group. A systematic error is observed in the X_2^+(0,a) and M_2^+ modes in the refinements performed against the PSD data.

temperature, the unit cell metric is clearly orthorhombic, which means the two most probable models are $Amam$ (X_3^-(a;0)) and $Pnnm$ (X_3^-(a;b) and M_2^+(a)), with additional superstructure peaks expected at (h+1, k+1, l+1) due to the M-point propagation vector for $Pnnm$. Our unbiased refinement with the $P2_1nm$ model reveals a systematic trend in mode amplitudes associated with M_2^+(a) Irrep point to the fact that the model is $Pnnm$. However, we were not able to find any superstructure peak in the data related to the M-point propagation vector. This is most likely due to the fact that only oxygen displacements enter in the M_2^+(a) Irrep whose contribution to the X-ray structure factor are very weak. However, in electron diffraction experiments performed on a sample with very similar chemical composition, $Ca_{2.10}Sr_{0.90}Ti_2O_7$, superlattice reflections corresponding to the M-point like $(010)_T$=$(110)_O$ and $(\frac{\bar{1}}{2}\frac{3}{2}0)_T = (210)_O$ in the temperature range from 473 to 700 K are observed [4]. Hence while we obtain only a slightly better refinement for our restricted $Pnnm$ model (Rwp = 9.17 and 15 degrees of freedom (DoF)) than with the $Amam$ (Rwp = 9.18 and 13 DoF), the observation of the superstructure peaks by electron diffraction in a closely related sample validates our assignment.

By 873 K the metric of the unit cell has evolved to be tetragonal within the high resolution of our experiment ($7x10^{-4}$ Å). The cell metric is no longer consistent with $Pnnm$ (or $Amam$) symmetry and signifies the occurrence of another crystallographically distinct phase, $P4_2/mnm$ (X_3^-(a;a), M_2^+(a)). At this temperature we still observe some weak superstructure peaks due to the X-point (see Fig. S6) and our unbiased refinements indicate a systematic evolution of the order parameters X_3^-(a;b) to X_3^-(a;a) and a non-vanishing M_2^+(a) order parameter (see Fig. S4 and Fig. 2d in the main text). In addition, the $P4_2/mnm$ model provides a superior fit of the data (Rwp = 9.13 and 13 DoF) than the aristotype $I4/mmm$ structure (Rwp = 9.16 and 6 DoF) without generating any spurious intensities in our model (see Fig. S6). At temperatures higher than 873 K, the superstructure peaks disappear (see Fig. S6) and the last phase transition to the aristotype $I4/mmm$ phase take place, in perfect agreement with the slope change observed in the thermal expansion coefficient showed in Fig. 2c in the main text.

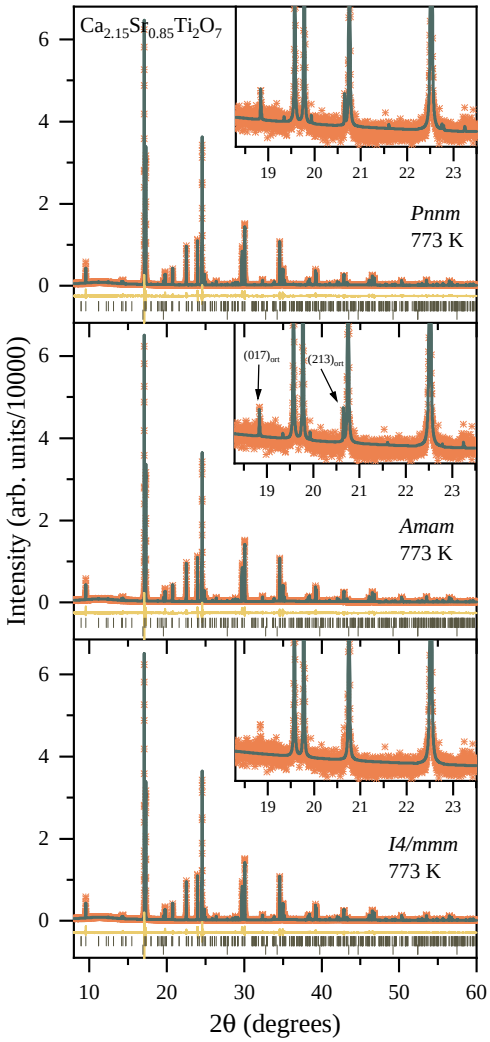

Figure S5. Rietveld fit to data collect on I11 for $Ca_{2.15}Sr_{0.85}Ti_2O_7$ at 773 K refined in the indicated models. Data points are plotted as orange crosses, Rietveld fit and differences as black and yellow lines respectively and black tick marks indicate symmetry allowed reflections. Inset shows enlarged region of the diffraction profile in the range 18-23 degrees. The arrows indicate two superstructure peaks due to the X-point expressed in the orthorhombic setting.

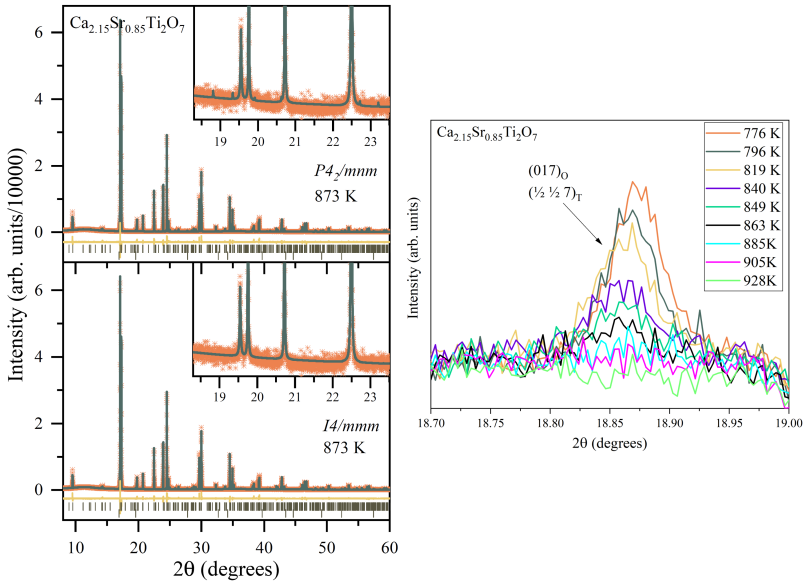

Figure S6. Left panel: Rietveld fit to data collect on I11 for $Ca_{2.15}Sr_{0.85}Ti_2O_7$ at 773 K refined in the indicated models. Data points are plotted as orange crosses, Rietveld fit and differences as black and yellow lines respectively and black tick marks indicate symmetry allowed reflections. Inset shows enlarged region of the diffraction profile in the range 18-23 degrees. Right panel: Thermal evolution of the intensity of the (017) superstructure reflection due to the X-point. This superstructure reflection is clearly observed until around 900 K. At temperatures higher than 900 K the last phase transition to the aristotype $I4/mmm$ phase take place.

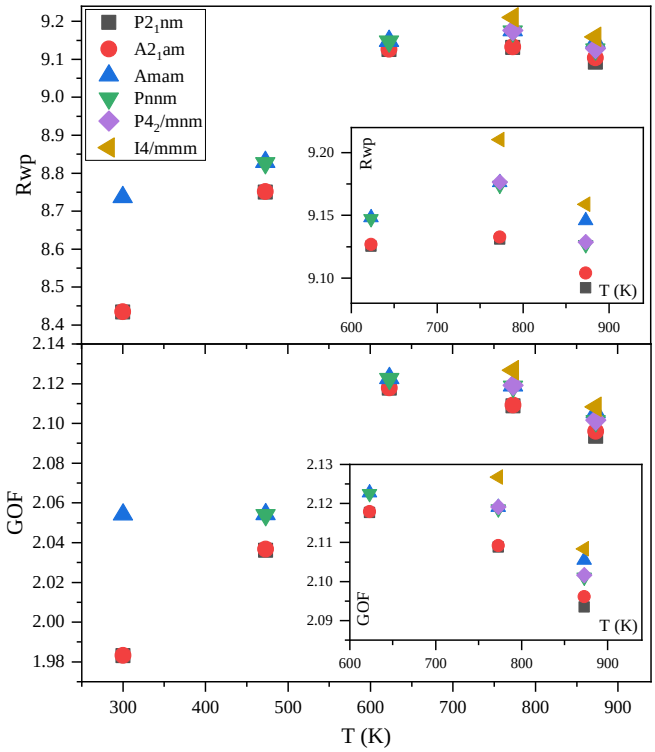

Figure S7. Agreement factors obtained for the refinements performed against the MAC data for $Ca_{2.15}Sr_{0.85}Ti_2O_7$ in the different analysed model for different temperatures.

II. DETAILS OF FIRST-PRINCIPLES SIMULATIONS

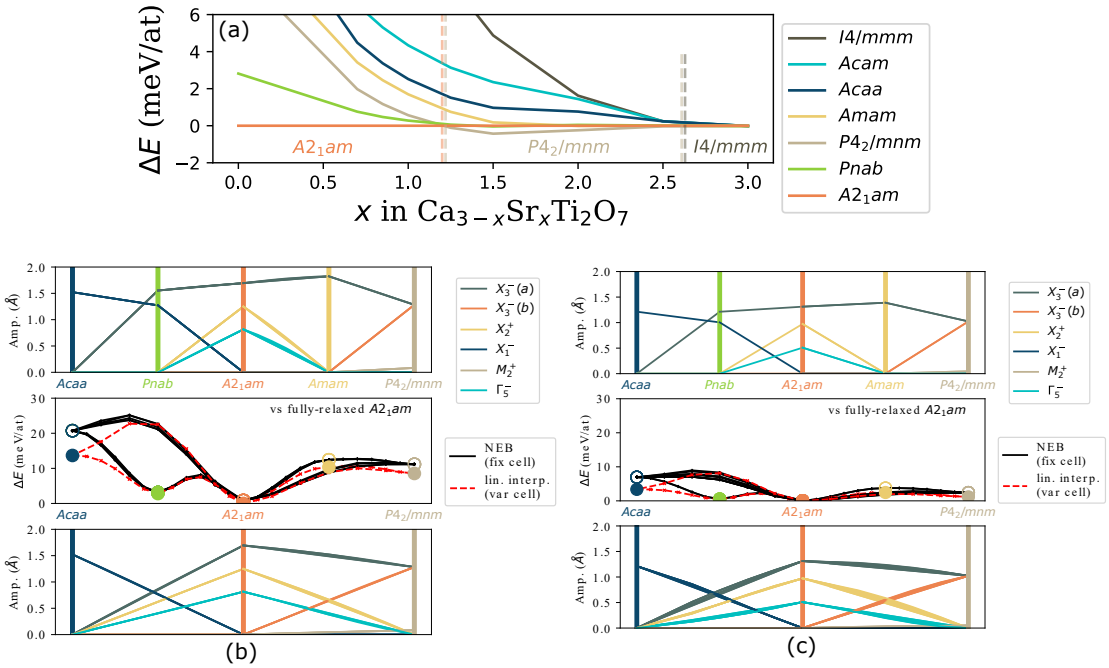

Figure S8. DFT simulation results: (a) energy difference of several Ruddlesden–Popper phases compared to the polar $A2_1am$ phase for $Ca_{3-x}Sr_xTi_2O_7$ compounds; (b) and (c) Transition pathways between the $A2_1am$ ground-state and various other phases for $Ca_3Ti_2O_7$ and $Ca_{2.15}Sr_{0.85}Ti_2O_7$, respectively. The middle panels of (b) and (c) show phase energies (relative to fully-relaxed $A2_1am$) of relaxed compounds with the $I4/mmm$ parent unit cell fixed (open circles) connected by transition pathways computed using a nudged elastic band (NEB) algorithm (black lines). Mode amplitudes, labelled according to their irreducible representation in the parent $I4/mmm$ phase, are displayed for two-step NEB pathways (top) and one-step NEB pathways (bottom). The width of these lines represent their change during the NEB optimisation. Results from all NEB iterations are shown. The middle plots also display the relative phase energies of fully-relaxed structures (closed circles) and the energies of connecting pathways found via linear interpolation of both cell strain and atomic positions.

Ca	3|2.0|9|10|12|30N:40N:31N:32N(qc=6)
Sr	3|2.0|4|5|6|40N:50N:41N:42N
Ti	3|1.8|15|17|19|30N:40N:31N:32N(qc=7)
O	1|1.2|23|26|31|20N:21L(qc=9)

Table S1. Pseudopotential strings used in all DFT calculations on $Ca_{3-x}Sr_xTi_2O_7$ Ruddlesden–Popper phases. All pseudopotentials are norm-conserving and generated on-the-fly within CASTEP version 16.0

In order to highlight the role of entropy in the phase transition taking place in $Ca_3Ti_2O_7$ and $Ca_{2.15}Sr_{0.85}Ti_2O_7$, we first computer the DFT ground-state transition pathways to compare how well this agrees with experimental results. We simulated the energetics of various possible transition pathways using the nudged elastic band (NEB) method [5]. Figures S8b and S8c show pathways connecting the $A2_1am$ phase (centre) to the $Acaa$ (left) and $P4_2/mnm$ (right) phases for $Ca_3Ti_2O_7$ and $Ca_{2.15}Sr_{0.85}Ti_2O_7$, respectively. Both one-step ($Acaa \leftarrow A2_1am$ & $A2_1am \rightarrow P4_2/mnm$) and two-step ($Acaa \leftarrow Pnab \leftarrow A2_1am$ & $A2_1am \rightarrow Amam \rightarrow P4_2/mnm$) transition pathways are considered. The middle panels plot energy (relative to the fully-relaxed $A2_1am$ ground state) for all transitions. The end-point phases for fixed cell boundary conditions (see Methods section) are shown as coloured open circles with black crosses connected by black lines showing the intermediate trajectories. The pathways for relaxed lattice parameters (see Methods section) are shown in Figures S8b and S8c (middle panel) as red dashed lines connecting filled circles representing phases with relaxed cells. This last pathway, since it is lowest in energy, will be discussed exclusively in the following section, and the significance of this step is particularly evident in the decrease in energy of the $Acaa$ relaxed structures.

For the transitions between the $A2_1am$ ground-state and $P4_2/mnm$ phases we considered in first place a one-step (direct) pathway connecting these phases (all intermediate trajectories are of the $P2_1nm$ space group, which is a common subgroup to both end phases). The energy increases monotonically along this $A2_1am \rightarrow [P2_1nm] \rightarrow P4_2/mnm$ minimum energy pathway (MEP) indicating no additional activation barrier to the energy difference between the end phases. An alternative two-step pathway via an $Amam$ intermediate also connects these phases. In the first $A2_1am \rightarrow Amam$ step, the X_2^+ rotation is lost and all but the final trajectories have $A2_1am$ symmetry. The energy increases monotonically with the loss of this rotation. In the second step, the X_3^- order parameter direction changes between $Amam$ ($X_3^-(a;0)$) and $P4_2/mnm$ ($X_3^-(a;a)$) and thus all trajectories along this path obey the symmetry operations of the $Pnnm$ ($X_3^-(a;b)$) space group. Within the space of order parameter directions spanned by the $X_3^-(a;b)$ irrep we see that the $Ca_3Ti_2O_7$ energy landscape resembles a bowed Mexican hat potential analogous to that identified in hexagonal manganites [6] (see Fig. S8). The MEP connecting the $Amam$ and $P4_2/mnm$ phases thus traces the well of this circular valley. In both compounds, the $Amam$ phase is greater in energy than $P4_2/mnm$ and in fact there is a very slight peak partway along the $Amam \rightarrow [Pnnm] \rightarrow P4_2/mnm$ path. DFT predicts the two-step transition pathway $A2_1am \rightarrow Amam \rightarrow Pnnm \rightarrow P4_2/mnm$ to have a higher activation barrier than a direct $A2_1am \rightarrow [P2_1nm] \rightarrow P4_2/mnm$ transition, although only by 1.31 meV/atom in $Ca_{2.15}Sr_{0.85}Ti_2O_7$. This is in good agreement with the continuous second order like transformation through intermediate $Amam$ and $Pnnm$ phases that we observe experimentally in $Ca_{2.15}Sr_{0.85}Ti_2O_7$. However, if we also consider the contribution from vibrational entropy at finite temperatures, we note that the $Amam$ phase has 13 DoF and the $Pnnm$ phase has 20; compared to 41 for $P2_1nm$. Since the energy difference between the pathways is almost negligible, it is understandable that the system undergoes a continuous transition via the higher entropy route.

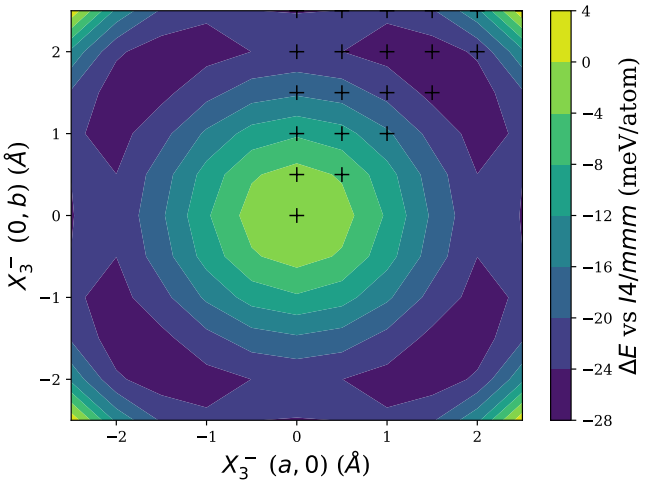

Figure S9. Energy landscape of distortions described by the $X_3^-(a;b)$ order parameter space in $Ca_3Ti_2O_7$. Black crosses show energies that were explicitly calculated, the remainder of the map was then formed using symmetry. Each $X_3^-(a;0)$ or $X_3^-(0;b)$ displacement has 6 degrees of freedom and thus the mean frozen displacement vector averaged across all $P4_2/mnm$ and $Amam$ phases throughout all compositions studied (extracted using amplimodes relative to the $I4/mmm$ parent) was frozen into the $I4/mmm$ $Ca_3Ti_2O_7$ structure using isodistort. All simulations had lattice parameters fixed to those of relaxed $I4/mmm$ (zero strain boundary conditions).

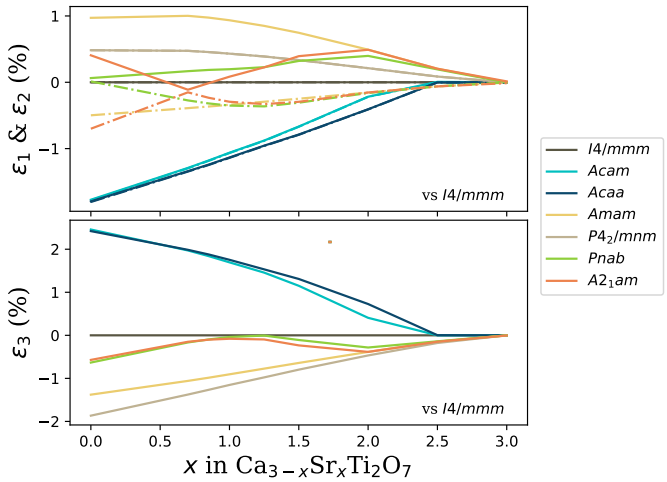

Figure S10. Strain in a (ε_1), b (ε_2) and c (ε_3) lattice parameters of different relaxed $Ca_{3-x}Sr_xTi_2O_7$ Ruddlesden–Popper phases as a function of x compared to the relaxed $I4/mmm$ aristotype. In the upper plot, when the ε_1 and ε_2 strains differ, the lower one is displayed as a dashed line.

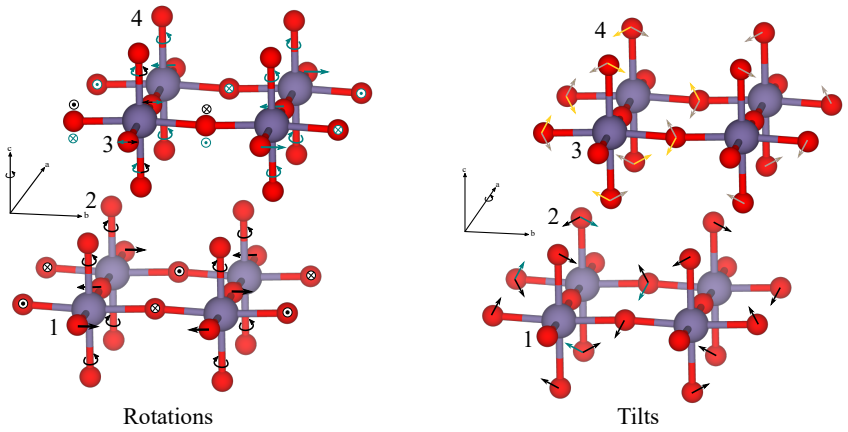

Figure S11. Figure showing diagrammatically, how in the n = 1 limit in RP phases, the AO layering means that tilts (right) have more degrees of freedom associated with them with rotations. Making a first choice (1) about the direction of rotation, fixes the direction of rotation within the layer (e.g. 2), leaving a single degree of freedom in the neighbouring layer (3). The depicted tilts on the other hand (i.e. rotations about the a axis) do not force octahedral 2, 3 or 4 to adopt any particular direction. Therefore in the n = 1 limit tilts have twice as many DOF as rotations.

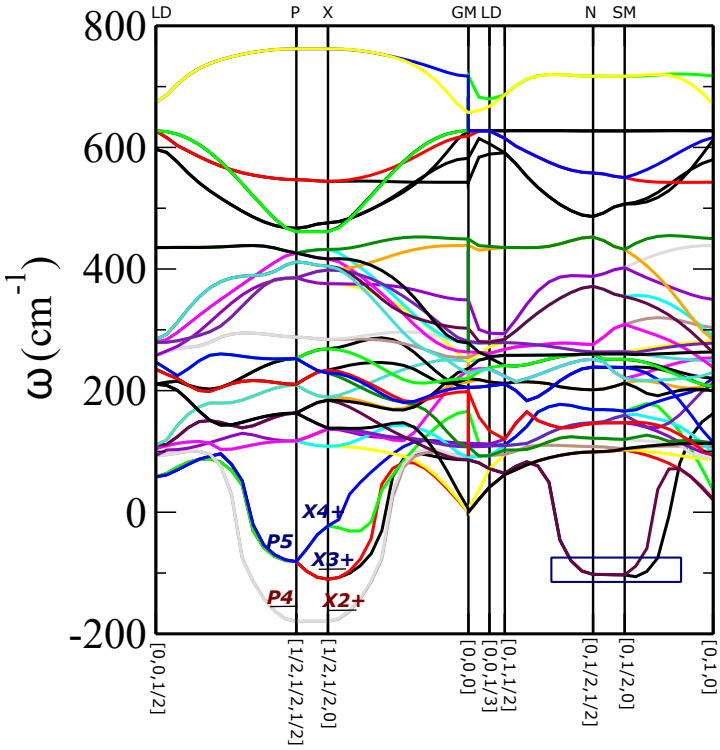

Figure S12. Phonon dispersion curve of Ca_2GeO_4 (RP1) illustrating the the consequences of the additional degrees of freedom described in Fig. S11. Tilt eigenvectors are labelled in blue and rotation in red. There is an additional band of low-lying eigenvectors with tilt character (blue box) on account of layering of the RP structure. This same layering does not however give rise to additional eigenvectors of rotation character.

[1] M. S. Senn, A. Bombardi, C. A. Murray, C. Vecchini, A. Scherillo, X. Luo, and S. W. Cheong, Physical Review Letters **114**, 23 (2015).
[2] M. S. Senn, C. A. Murray, X. Luo, L. Wang, F. T. Huang, S. W. Cheong, A. Bombardi, C. Ablitt, A. A. Mostofi, and N. C. Bristowe, Journal of the American Chemical Society **138**, 5479 (2016).
[3] H. T. Stokes and D. M. Hatch, J. Appl. Cryst. **38**, 237 (2005).
[4] F.-T. Huang, B. Gao, J.-W. Kim, X. Luo, Y. Wang, M.-W. Chu, C.-K. Chang, and H.-S. Sheu, npj Quantum Materials **1**, 16017 (2016).
[5] G. Henkelman and H. Jónsson, The Journal of Chemical Physics **113**, 9978 (2000).
[6] S. Griffin, M. Lilienblum, K. Delaney, Y. Kumagai, M. Fiebig, and N. Spaldin, Physical Review X **2** (2012).